coatings

MDPI

Review

Dual-Mechanism Synergistic Regulation and Performance Optimization of Lead Sulfide Quantum Dot Coatings in Optoelectronic Memristors

Ru Li [1], Xinhe Jiang [1], Xuhao Zhao [1], Huiyun Zhang [2], Qingyu Xu [3] and Guangyu Wang [1,*]

[1] School of Physics Science & Information Technology, Liaocheng University, Liaocheng 252059, China
[2] School of Materials Science and Engineering, Shanxi Normal University, Taiyuan 030031, China
[3] School of Physics, Southeast University, Nanjing 211189, China
* Correspondence: wangguangyu@lcu.edu.cn

Abstract

Lead sulfide quantum dots (PbS QDs), as a functional-layer coating, enable non-volatile integration and neuromorphic computing in memristive structures to address the von Neumann bottleneck. Herein, the dual-interface mechanism of PbS QDs in the memristor film structure is reviewed. First, the local electric field enhancement effect generates tip electrode-like structures in the coating film through QD-mediated spatial charge gradients, thereby enabling precise control over the nucleation and growth of conductive filaments (CFs). As a result, the consistency of switching voltages and the thermal stability at elevated temperatures are significantly improved. Conversely, the anion reservoir effect exploits surface dangling bonds on QDs to efficiently capture anions from the dielectric layer, thereby synergistically regulating vacancy migration kinetics. This process enables zero-initialization behavior and ultra-low-power operation. In addition, the spatial distribution design and density modulation of QDs further reinforce both mechanisms. The structural optimization of QD/dielectric interface engineering can simultaneously improve cycling endurance and resistive switching uniformity. Furthermore, modification of QD surface chemistry through ligand decoration and passivation suppresses the stochasticity of ionic diffusion while improving the linearity of synaptic weight updates. This interfacial engineering strategy utilizing QDs as coating films advances the development of high-performance photonic–electronic systems for memory–computing convergence.

Keywords: lead sulfide quantum dot; optoelectronic memristors; local electric field enhancement; anion reservoir

Check for updates

Academic Editor: Dimitrios Tasis

Received: 2 May 2026
Revised: 10 June 2026
Accepted: 11 June 2026
Published: 15 June 2026

Copyright: © 2026 by the authors. Licensee MDPI, Basel, Switzerland. This article is an open access article distributed under the terms and conditions of the Creative Commons Attribution (CC BY) license.

1. Introduction

The conventional von Neumann architecture, which is inherently constrained by the physical separation of computing and memory units, faces severe performance bottlenecks in the era of big data and artificial intelligence [1–3]. This structural limitation restricts the ability to satisfy the growing demands for high-density data storage and high-speed information processing [4–6]. Addressing this challenge requires the development of in-memory computing technologies, which in turn depend on novel memory devices that are compatible with on-chip integration and possess high density, non-volatility, and fast operation [7–11].

The memristor, proposed by Leon Chua in 1971 as the fourth fundamental passive circuit element after the resistor, capacitor, and inductor, is essentially a resistor charac-

terized by a constitutive relationship between charge and flux linkage [12–15]. Owing to its non-volatility, intrinsic memory–computing integration capability, low power consumption, and synapse-like bioinspired characteristics, the memristor shows strong adaptability to both digital and analog computing paradigms [16–19]. As a result, it has become a key hardware platform for storage–computing convergence and neuromorphic computing, providing an important technological route to overcome the von Neumann bottleneck, meet the requirements of in-memory computing, and improve computational performance in the post-Moore era [20–25].

A typical memristor consists of top and bottom electrodes combined with a functional layer, and its performance is strongly determined by the properties of the functional material [26,27]. QDs have attracted significant attention as promising candidates for this layer due to their tunable optoelectronic properties, pronounced quantum confinement effects, and excellent interfacial compatibility [28–31]. Extensive studies have validated II–VI and III–V group QDs alongside perovskite-based variants for such applications [32–34]. Material engineering strategies further enhance QD functionality: dual doping in II–VI QDs enables precise band structure and carrier dynamics control [35]; PbSe/CdSe point-sheet heterostructures facilitate ultrafast exciton transfer through level matching [36]; Cu doping introduces interband states and magneto-optical responses for fine resistance regulation [37]; and single-particle fluorescence spectroscopy elucidates doping valence states and resistive switching mechanisms [38]. Moreover, QDs demonstrate proven efficacy in photodetectors and solar cells, where PbS QDs exhibit enhanced performance via surface restructuring and defect passivation [39]. Notably, group IV–VI PbS QDs surpass II–VI, III–V, and perovskite counterparts in resistive memory and artificial synaptic applications owing to their broadly tunable bandgap (1.0–1.6 eV), exceptional solution processability, robust quantum confinement, and superior environmental stability [40–42].

The results of existing studies have demonstrated that memristors incorporating PbS QDs can significantly reduce power consumption while improving the uniformity of switching parameters [43–45]. These advantages make PbS QDs an attractive platform for enhancing memristor performance and developing next-generation computing hardware with high energy efficiency, parallel processing capability, and sensing functionality [46,47]. Therefore, a comprehensive understanding of the mechanisms by which PbS QDs improve memristor performance remains essential [48–51]. In this paper systematically, we review the effects of PbS QDs on memristor performance and recent application advances, with particular emphasis on the underlying optimization mechanisms, particularly the local electric field enhancement effect and the anion reservoir mechanism (Figure 1). Current challenges are also discussed, and future research directions are outlined to provide theoretical reference and support for further progress in this field.

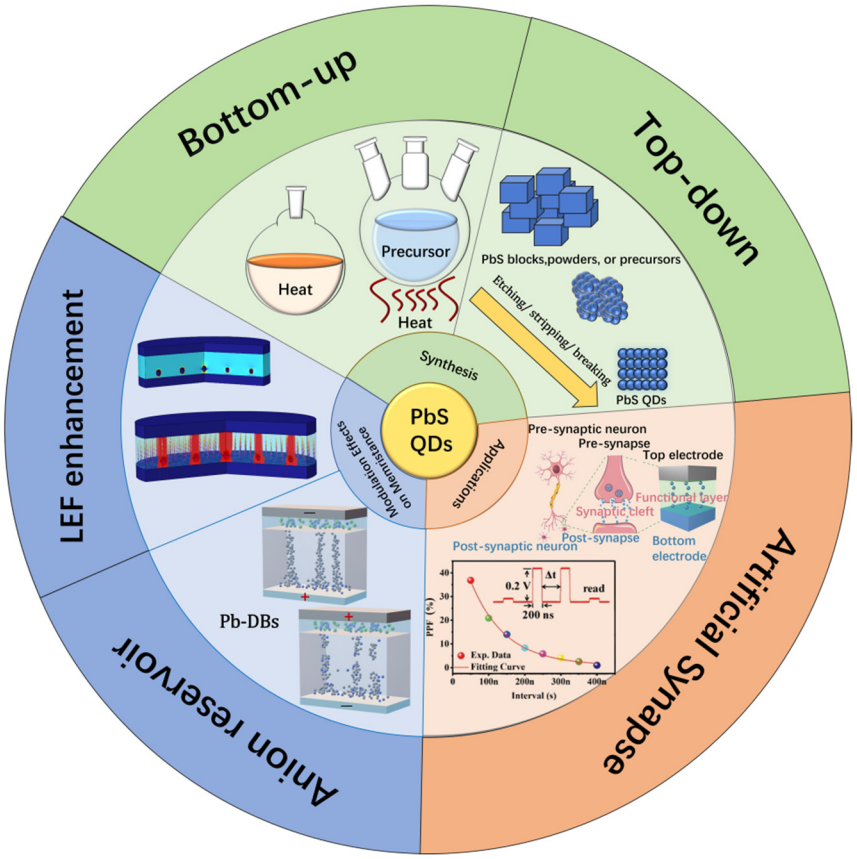


Figure 1. Overview of synthesis of PbS QDs, the regulatory effects on memristors, and applications in artificial synapses. Artificial synapse. Reprinted (adapted) with permission [48]. Copyright 2019, Wiley-VCH. Reprinted (adapted) with permission [52]. Copyright 2023, Wiley-VCH.

2. Characteristics and Synthesis Methods of PbS QDs

2.1. Characteristics of PbS QDs

PbS QDs are quasi-zero-dimensional nanomaterials with considerable application potential [53,54]. The results of previous studies have demonstrated that their size can be precisely tuned from 2.9 nm to 6.1 nm through controlled synthesis (Figure 2a–i) [55]. The surface of PbS QDs contains abundant lead dangling bonds (Pb-DBs), which enable efficient capture and storage of anions [56]. In addition, ligand modification, with, for example, EDT, TBAI, and PbI_2, effectively regulates the surface properties and bandgap of PbS QDs [57–61]. Owing to an exciton Bohr radius of approximately 18 nm, PbS QDs exhibit pronounced quantum confinement effects, allowing the bandgap to be tuned over the range of 0.6–1.6 eV [62,63]. Their absorption spectrum extends from the ultraviolet to the short-wave infrared region (Figure 2j) [64]. Moreover, high sensitivity to near-infrared light at 750 nm and 1650 nm has been demonstrated [54,62], enabling optical signal detection in complex environments [65,66]. As a result, PbS QDs have attracted increasing attention in intelligent sensing, artificial synapses, and flexible electronics [67,68].

2.2. Synthesis Method of PbS QDs

The synthesis of PbS QDs mainly relies on two fundamental strategies: top-down and bottom-up approaches. These two routes differ in synthetic pathway, product characteristics, and application scope and together provide the basis for the precise preparation and functional development of PbS QDs.

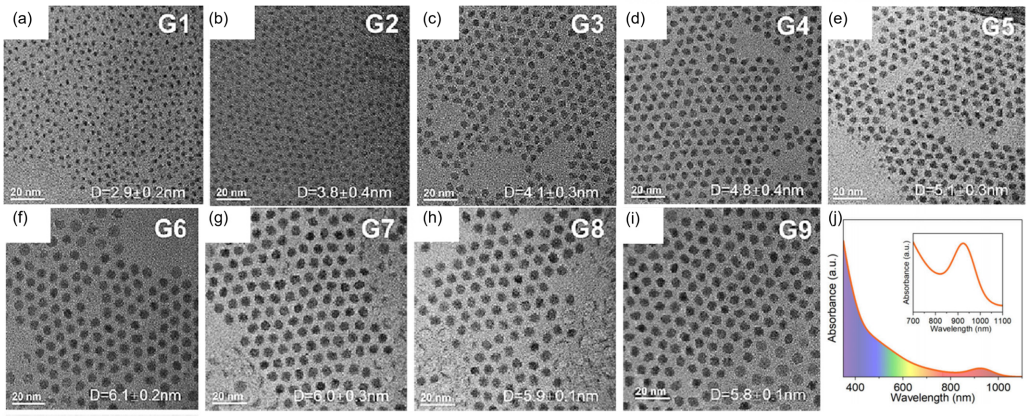


Figure 2. (**a**–**i**) Particle size and morphology evolution of PbS QDs observed from TEM images. Reprinted (adapted) with permission [55]. Copyright 2026, American Chemical Society. (**j**) Absorption spectrum of PbS QDs covering UV–visible-NIR regions. Reprinted (adapted) with permission [64]. Copyright 2025, American Chemical Society.

2.2.1. Top-Down

In the top-down approach, Macroscopic PbS materials, including bulk solids, powders, or precursors, are converted into nanoscale QDs or nanocrystals through physical or chemical processes such as etching, exfoliation, fragmentation, and size regulation [62]. A representative method reported by Yang et al. involves millisecond pulsed laser irradiation of polydisperse PbS nanocrystal suspensions to achieve size selection through the quantum confinement effect (Figure 3a–c) [69]. Precise regulation of the water bath temperature controls the particle size and induces a photoluminescence blue shift from 1427 nm to 1060 nm as the particle size decreases. The resulting high-purity QDs are suitable for advanced electronic applications. In another example, Liu et al. developed a chemical cracking method based on micrometer-sized Pb(OH)Cl precursors [70]. In this process, the synergistic effect of oleic acid and oleylamine (OLA) generates an active intermediate that subsequently reacts with sulfur sources, and the following aging treatment produces QDs with sizes of 4.8–8.3 nm (Figure 3d,e) and a quantum yield of 35.9% (Figure 3f). This method shows the advantages of both operational simplicity and environmental friendliness.

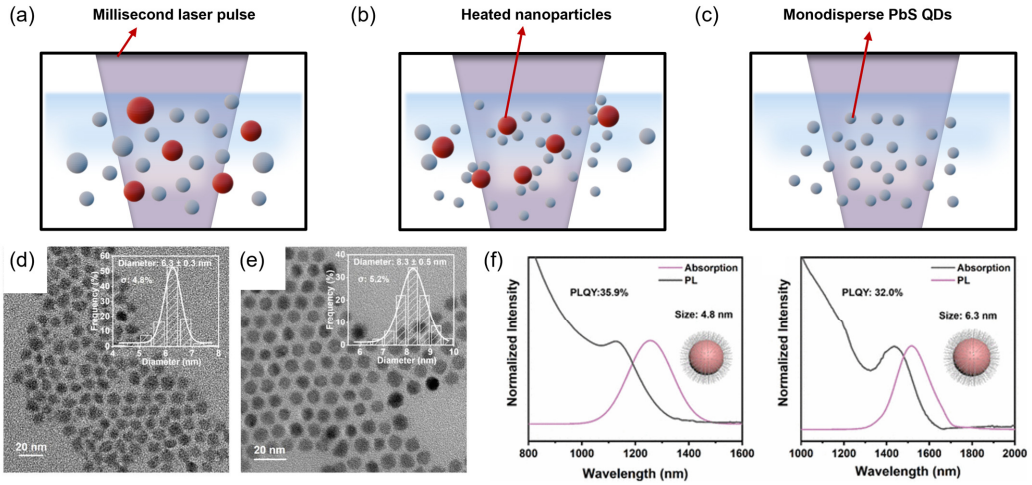


Figure 3. (**a**) Selective heating of large nanoparticles. (**b**) Further selective heating after vaporization and condensation. (**c**) Formation of monodisperse PbS QDs. TEM images of PbS QDs prepared under different conditions: (**d**) T_a = 120 °C, T_b = 70 °C, t = 20 min; (**e**) T_a = 120 °C, T_b = 160 °C, t = 20 min. (**f**) Absorption and PL spectra of typical PbS QDs. Reprinted (adapted) with permission [70]. Copyright 2024, American Chemical Society.

2.2.2. Bottom-Up

The bottom-up strategy begins with molecular or atomic Pb and S precursors, which self-assemble into nanoscale PbS materials, such as QDs and nanocrystals, through chemical bonding, nucleation, and growth processes [62,71]. In the conventional thermal injection method, a non-metal precursor solution is rapidly injected into a high-temperature metal precursor solution under an inert atmosphere to trigger the nucleation and growth of QDs; this process is often combined with ligand modification to regulate material properties [72]. In contrast, the non-injection method reported by Pan et al. uses $PbCl_2$ and sulfur powder, preferably thioacetamide (TAA), as precursors, with OLA serving as both the ligand and solvent at defined molar ratios (Figure 4a) [73]. Controlled heating and quenching promote nucleation in accordance with the LaMer model, producing QDs with a size dispersion below 9%. Both particle size and bandgap can be tuned by adjusting the reaction temperature (Figure 4b–d), with this method offering the additional advantages of mild reaction conditions and operational simplicity.

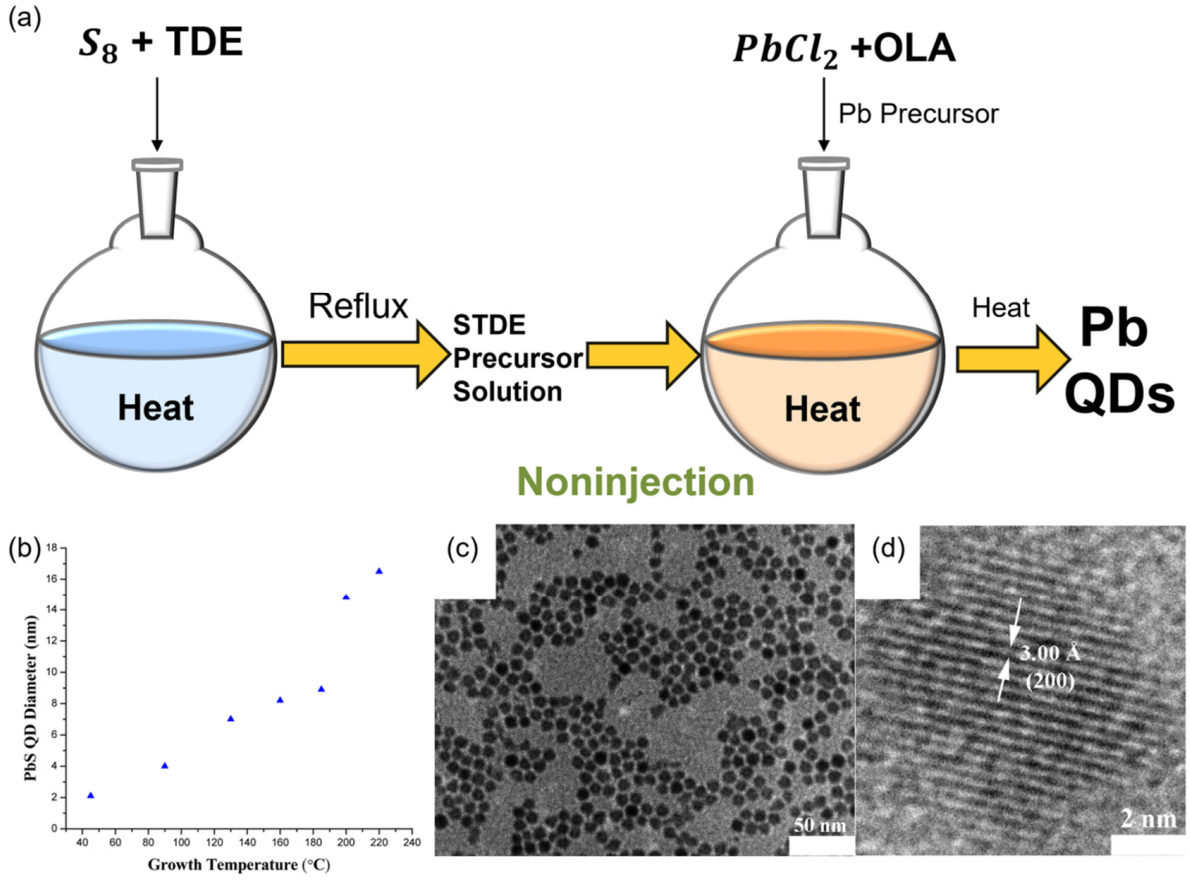


Figure 4. (**a**) Non-injection synthesis of PbS QDs. (**b**) Temperature dependent on measured diameters of PbS QDs synthesized using the non-injection approach. (**c**) TEM image of QDs, with a size of 7.0 ± 0.5 nm. (**d**) High-resolution TEM (HRTEM) image of QDs. Reprinted (adapted) with permission [73]. Copyright 2015, American Chemical Society.

The coordinated development of top-down and bottom-up synthesis strategies has enabled precise control over key parameters of PbS QDs, including size and bandgap, thereby effectively addressing the poor product uniformity and limited performance controllability associated with single-method fabrication routes. This progress provides a solid material basis for the performance optimization, structural design, and large-scale implementation of PbS QD-based memristors.

3. The Modulation Effects of PbS QDs on Memristors

Oxide, nitride, and perovskite systems have been extensively investigated as functional layers for memristive devices, exhibiting distinct ion migration mechanisms [2,32,74,75]. In oxide systems, CFs form through directional migration and accumulation of oxygen vacancies along lattice defects. Nitride systems rely on coordinated transport of nitrogen vacancies and metal interstitial atoms to establish conductive channels, while perovskites facilitate low-activation-energy halide ion migration under electric fields. QD variants employ material-specific switching principles: Oxide QDs utilize oxygen vacancy charge traps for resistance modulation via charge trapping/desorption [2]; $CsPbBr_3$ QDs regulate carrier transport through multi-ion migration ($Br^-/O^{2-}/Ag^+$), interfacial Schottky barriers, and photo-induced built-in fields enabling optoelectronic dual-control [32]; Nitride QDs primarily exploit electron trap storage effects for resistive switching [74].

In contrast, PbS QDs leverage localized electric field enhancement and anionic reservoir mechanisms [48–51]. Local tip fields concentrated around particles significantly reduce migration barriers for anions (N^{3-}/O^{2-}) and active cations (Ag^+) within dielectric matrices, while surface Pb dangling bonds anchor excess anions to stabilize vacancy distributions—enabling precise conductive filament nucleation. Under forward bias, anion capture at QD interfaces generates in situ vacancies, directing metal ion aggregation into filaments along optimized field paths; reverse bias triggers anion desorption and filament fracture through ionic retracing.

Resistance modulation varies significantly across QD memristors (Table 1): CdSe QDs utilize abundant surface defect traps, $CsPbBr_3$ employs ion migration-photoelectric synergy, graphene QDs modulate oxygen vacancies, and carbon QDs exploit surface functional group trapping. PbS QDs surpass conventional QD devices (>1.6 V threshold) by coordinating field focusing with anion reservoir capabilities to achieve sub-1.0 V reversible switching.

Table 1. Comparison of the key performance parameters of various QD memristors.

Structure	Switching Mechanism	R_{ON}/R_{OFF}	V_{SET}/V_{RESET} (V)	Endurance (cycles)	Retention (s)	Synaptic Indicators	Refs.
Ag/Ga_2O_3/PbS QDs(NQDs)/Pt	ECM/SCLC	10^6	+0.19/−0.12	10^9	10^6	LTP LTD STDP PPF	[48]
Ag/QDHP-2(QDHP-4)/Ag	ECM/SCLC	>10	—	10^2	10^3	—	[49]
Ta/PbS QDs/AlOXNY/Pt	VCM/SCLC/TCM	10^2	<+1.0/>−1.0	>600	10^3	—	[50]
Pt/AlN/PbS QDs/Ta	VCM/SCLC/TCM	10	+0.5~+0.7/−1.0	10^3	700	—	[51]
ITO/CdS@PbS/Al	TCM/IBM	1.96	+0.95/−0.92	—	—	—	[49]
Ag/PbS QDs@PMMA/ITO	ECM/SCLC	10^4	+1.1/−1.1	10^2	>10^4	—	[76]
Glass/ITO/ZnO/PbS QDs/ZnO/Al	VCM/TCM	50~100	—	10^3 (electric pulse)	>150	SRDP EPSC IPSC PPF PTP PPD PTD	[77]
Al/PbS QDs/ZnO QDs/ CuSCN/PEDOT:PSS/ ITO/Glass	TCM/IBM	—	—	250 (light pulse)	>10^2	EPSC STP	[64]
Al/PVA/PbS QDs/ITO	IBM/TCM	10^3	—	—	10^3	—	[44]

Table 1. *Cont.*

Structure	Switching Mechanism	R_{ON}/R_{OFF}	V_{SET}/V_{RESET} (V)	Endurance (cycles)	Retention (s)	Synaptic Indicators	Refs.
Al/PVA/PbS:Cu QD/ITO	TCM/IBM	10^2~10^3	—	—	—	—	[78]
Ag/MoO_3/PbS QDs(EDT/TBAI)/ZnO NPs/ITO/Glass	ECM/SCLC	10^2	+1.0/−1.0	10^2	—	EPSC PPF STM LTM	[79]
Al/$CsPbBr_3$ QDs/MoS_2/FTO	SCLC/TCM	12	+1.0/−1.0	—	10^2	—	[80]
Ag/$CsPbBr_3$ QDs:GO/ITO (dark)	ECM/VCM/IBM	10^4	+2.28/−2.04	10^2	>10^3	—	[32]
Ag/$CsPbBr_3$ QDs:GO/ITO (illumination)	ECM/VCM/IBM	10^7	+1.68/−1.08	10^2	>10^3	—	[32]
ITO/$CsPbBr_3$ QDs/Au	VCM/SCLC	10^7	+1.55/−2.4	—	10^3	—	[75]
Ag/PMMA&0.5% CQDs/FTO	ECM/TCM	>150	+1.1/−1.025	10^2	10^4	—	[81]
Ag/CQDs@ Neem/FTO	ECM/TCM/ SCLC/IBM	10	+1.68/−2.28	10^2	>10^3	—	[82]
Au/CQDs/ITO	TCM/IBM	—	+1.009/−1.193	10^2	—	EPSC LTP LTD STDP	[83]
Pt/CQDs-Indigo/Pt	TCM/SCLC	10^1~10^2	+1.66/−1.55	≥1250	—	EPSC LTP LTD	[84]
ITO/PEDOT-PSS:GO-QDs/Al	TCM/SCLC/IBM	10^4	+2.1/ −2.0	10^2	>10^4	—	[85]
Ag/PVP-MXene QDs/Si	ECM/TCM	10^5	+2.4/ −1.3	—	—	EPSC LIF	[86]
ITO/CdSe QDs-PVP/Al	TCM/SCLC	10^5	+1.6/−1.7	>4000	>10^3	—	[87]
Al/PVP-CdSe QD/Al	TCM/SCLC	10^4	+0.61/−0.5	150	10^5	—	[33]
Ag/Galatin:CdSe/ZnS /ITO/Glass	ECM/SCLC/TCM	10^5	+1.8~+2.75/ −1.35~−0.25	10^2	>10^4	—	[88]

PbS memristor behavior critically depends on electrodes: Ag-active electrodes enable electrochemical metallization (ECM)-coupled space-charge-limited current (SCLC) modulation via Ag^+ migration and metallic filament formation, whereas inert electrodes (e.g., Au, Pt) promote defect charge trapping. Material modifications further induce multi-mechanism synergy: Oxide incorporation introduces oxygen vacancies for valence change memory (VCM)-enhanced stability; polymer interlayers suppress ECM by blocking ion diffusion, shifting control to interface barriers; heterostructures exploit multi-level interfacial traps. These tailored mechanisms govern synaptic performance, with multi-mechanism coupling enabling balanced long-/short-term biomimetic responses—establishing the core design principle for PbS-based photonic synapses.

3.1. Local Electric Field Enhancement Effect of PbS QDs

The non-uniform charge distribution within the PbS QD functional layer enhances the local electric field, resulting in a significantly higher field intensity in the vicinity of the QDs than in the surrounding regions. This field concentration effect generates a tip

electrode-like configuration around the PbS QDs, thereby directing the nucleation sites and growth orientation of CFs. As a consequence, the distribution of switching voltages becomes narrower, and the regulation performance of the memristor is improved.

Yan et al. (2019) demonstrated that Ag/Ga_2O_3/networked PbS QD (NQD)/Pt devices significantly outperformed Ag/Ga_2O_3/Pt control devices (Figure 5a) [48]. The NQD-containing devices exhibited narrower set voltage and reset voltage ranges, with V_{set} values of 0.12–0.26 V and V_{reset} values of −0.19 to −0.05 V. Their average threshold voltages were 0.19 V for V_{set} and −0.12 V for V_{reset} (Figure 5b), which were markedly lower than those of dispersed QD (IQD) devices, at 0.84 V and −0.83 V, respectively (Figure 5c). In addition, the NQD MDs exhibited much lower power consumption than the other two MDs (Figure 5d). The NQD structure strengthens the local electric field and promotes the selective accumulation of Ag^+ at QD sites, thereby guiding CF growth and enabling precise regulation of memristor characteristics. Temperature-dependent resistance ratio (R/R_o) measurements yielded a slope of 4.23 × 10^{-3} K^{-1}, which agrees well with the theoretical value for defective Ag nanowires with a diameter of 30 nm (4 × 10^{-3} K^{-1}), confirming the dominant role of Ag CFs in resistive switching (Figure 5e,f).

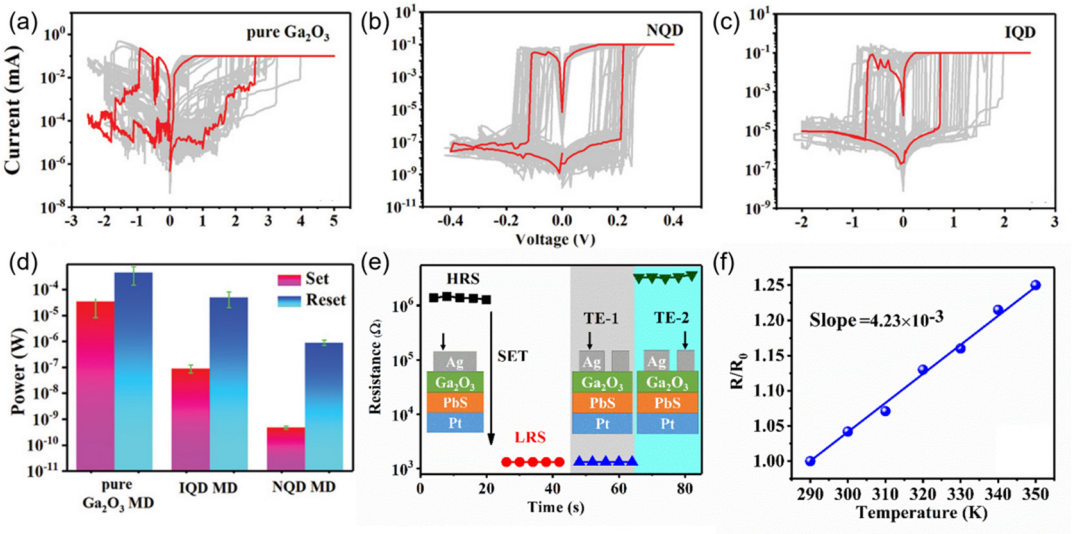


Figure 5. (**a**–**c**) Endurance of I–V characteristics for different device batches. (**a**) Pure-Ga_2O_3 MDs, (**b**) NQD MDs, and (**c**) IQD MDs. (**d**) Switching power of the three types of MDs. The error bars denote the minimum and maximum values measured for each category. (**e**) Resistances measured for various configurations. The top electrode was divided into TE-1 and TE-2 using the probe tip after the cell was switched from the HRS to LRS via the set process. (**f**) Relationship between resistance and temperature. Reprinted (adapted) with permission [48]. Copyright 2019, Wiley-VCH.

Younis et al. (2020) investigated $MAPbBr_3$ perovskite memristors incorporating colloidal PbS QDs at concentrations of 2 wt% (QDHP-2) and 4 wt% (QDHP-4) (Figure 6a) [49]. Pure $MAPbBr_3$ devices exhibited negative differential resistance (NDR) only at room temperature and showed no obvious resistive switching behavior. By contrast, the QDHP devices displayed stable filamentary resistive switching at elevated temperatures (Figure 6b–d). Electrode cutting experiments localized the low-resistance state to the CF region, confirming the metallic nature of the conductive pathway. In situ optical imaging and PL mapping further directly visualized the dynamic processes of Ag electrode dissolution, Ag^+ migration, and Ag-CF formation (Figure 6e,f). In addition, QDHP-4 reduced the activation energy to 0.54 eV, compared with 0.67 eV for $MAPbBr_3$, thereby improving charge transport efficiency and eliminating I–V hysteresis. After 8000 s at 100 °C, the

resistance of QDHP-2 remained stable, whereas that of the pure perovskite device doubled and showed pronounced fluctuations.

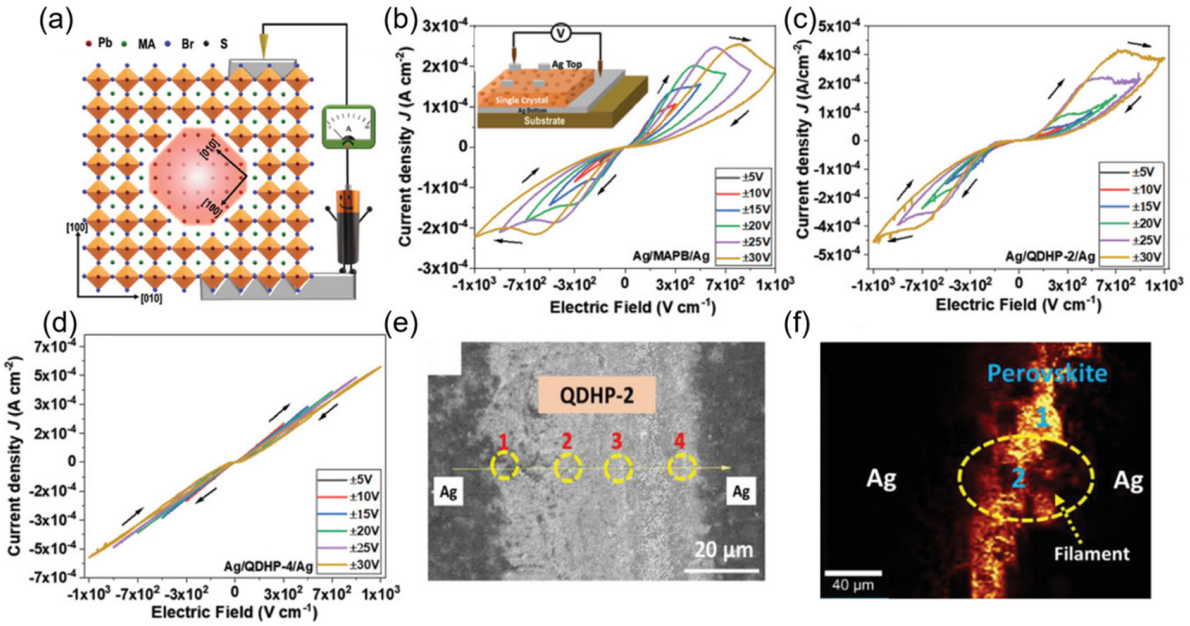


Figure 6. (**a**) Schematic illustration of the atomistic model of the PbS QDs/perovskite lattice-anchored heterostructure material system and the corresponding device structure. I–V characteristics measured at different sweep voltage ranges (0V-5V-0V--5V-0V) for (**b**) $MAPbBr_3$, (**c**) QDHP-2, and (**d**) QDHP-4 at room temperature. (**e**) SEM image of the device in the ON state. The arrow shows the direction of the electric field used to switch the device into the SET state (1 to 4 represent four different marked locations). (**f**) PL mapping of the channel in the ON state. The bright (marked as 1) and the dark (marked as 2) positions represent the perovskite-rich and the Ag-rich regions, respectively. Reprinted (adapted) with permission [49]. Copyright 2020, Wiley-VCH.

To investigate localized electric field enhancement triggered by PbS QDs, we constructed a simulation model of a single device using COMSOL Multiphysics 5.5 and performed finite element simulations, with the aim of analyzing the electric field varies at individual QDs under electrical excitation. The modeled geometry comprised two electrode layers and a perovskite active layer. The simulated structure comprises two electrodes sandwiching a 50 nm thick perovskite active layer, with total device dimensions of 300 nm. Electrodes were modeled at 20 nm thickness, while PbS QDs (6 nm diameter) were distributed at 60 nm intervals. Two configurations were analyzed: vertical offset by 5 nm from the FTO electrode and symmetric *z*-axis positioning. A 1 V bias was applied to the top electrode with the bottom electrode grounded, explicitly excluding thermal perturbations to isolate electrostatic contributions. The computational domain employed physics-controlled meshing with a minimum element size of 0.6654 nm and average mesh quality of 0.6407. Comsol simulation results demonstrate significant localized electric field enhancement near PbS QDs (Figure 7a), providing mechanistic support for the preferential CF formation along enhanced field vectors (Figure 7b). Consequently, switching voltage distributions narrowed and memristor performance improved. Spatial variation of PbS QDs within the functional layer demonstrated persistent field localization (Figure 7c); however, field magnitudes near QDs decreased monotonically with increasing distance from the bottom electrode (Figure 7d).

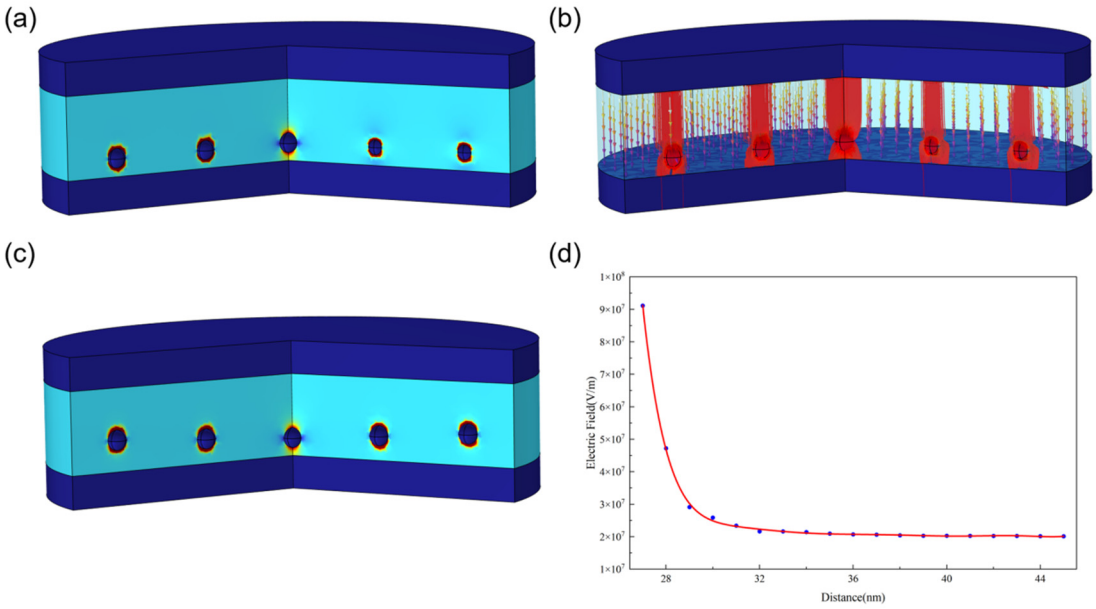


Figure 7. (**a**) Three-dimensional electric field distribution. (**b**) Internal electric field flow lines in the functional layer. (**c**) Electric field enhancement under varying QD spatial distributions. (**d**) Distance-dependent electric field intensity at QD positions relative to the bottom electrode.

PbS QDs act as efficient charge-trapping centers that enhance the local electric field and thereby enable precise regulation of memristor behavior. The resultant field concentration directs the nucleation and growth of CFs at designated locations through the combined effects of electric field focusing and ion transport channel optimization. This mechanism significantly improves the spatial controllability of CF formation and rupture, leading to a narrower distribution of switching voltages. In addition, it facilitates repeated CF growth along predefined pathways, reduces the risk of random filament fracture, and substantially improves cycling stability under thermal stress. More importantly, in materials with weak intrinsic resistive switching capability, such as pure perovskites, PbS QDs can induce stable filamentary switching behavior. Therefore, the local electric field enhancement effect is a fundamental mechanism by which switching consistency, environmental stability, and controllability are improved in memristive devices.

3.2. The Anionic Reservoir Effect of PbS QDs

PbS QDs have become an important functional material for improving memristor performance because of their distinctive anion reservoir properties. This behavior originates from the abundant lead dangling bonds (Pb-DBs) on the QD surface, which can effectively capture and store anions, such as N^{3-} and O^{2-}, thereby forming a natural anion reservoir. This mechanism was experimentally confirmed by Tamara Sloboda et al. via hard X-ray photoelectron spectroscopy (HAXPES) tests demonstrating Pb-DB interactions with I^{-}, Br^{-}, and O^{2-} ions [77]. In combination with the local electric field enhancement effect, this feature significantly regulates the growth behavior of CFs, leading to reduced operating voltage and suppressed volatility.

Sun et al. and Duan et al. independently clarified the synergistic modulation mechanism of PbS QDs in memristors through structural optimization [50,51]. Sun et al. systematically investigated the positional effect of PbS QDs in the device and found that the Ta/PbS QDs/AlO_xN_y/Pt structure takes advantage of the functional alignment between the anion reservoir effect of Pb-DBs in the QD film and the intrinsic reservoir effect of the Ta electrode. This synergistic interaction significantly lowers the set and reset voltages and enables forming-free operation. The optimal performance was obtained at an

intermediate QD film thickness of 4.5–7.5 nm, which was characterized by a substantial reduction in threshold voltage, low current fluctuation, and a large resistive switching ratio. In parallel, Duan et al. developed a Pt/AlN/PbS QDs/Ta memristor and analyzed it using high-angle ring-shaped dark-field (HAADF) technique combined with energy dispersive spectroscopy (EDS) on scanning transmission electron microscopy (STEM). The results revealed significant spatial overlap between Pb and nitrogen atoms at the AlN/PbS QDs interface, directly demonstrating that nitrogen ions were captured and stored within the PbS QDs layer. Under electric field stimulation, N^{3-} ions in AlN migrate and are captured by Pb-DBs, forming nitrogen vacancies (V_N) in situ and increasing the defect concentration in the system, thereby achieving memristive behavior with no or low formation voltage. When a bias is applied, some N^{3-} ions are captured by Pb-DBs while others migrate to the Ta electrode to form TaN, with the nitrogen vacancies serving as low-resistance conductive pathways. N^{3-} capture induces lattice charge imbalance, generating vacancies; under reverse electric field, N^{3-} desorb and reoccupy these vacancies, thus restoring the resistive state. Together with local electric field enhancement, this process directs CF growth and gives rise to forming-free characteristics, with stable set and reset voltages of 0.5–0.7 V and −1 V, respectively. It is noteworthy that excessively low concentrations of PbS QDs result in insufficient nitrogen ion capture, low defect concentration, and random growth of CFs; conversely, high concentrations lead to excessive capture and distortion of interfacial barriers, preventing complete isolation of conductive pathways and reducing the on/off ratio. Further optimization of the QD concentration, with 5 mg/mL giving the best performance, resulted in stable switching over 150 cycles and endurance up to 3000 cycles. Taken together, the results of these studies demonstrate that rational tuning of the position, thickness, or concentration of PbS QDs can simultaneously exploit the anion reservoir effect and local electric field enhancement, thereby markedly reducing threshold voltage and power consumption and providing an effective strategy for the design of high-performance, low-power memristors.

Surface Pb-DBs allow PbS QDs to function as anion reservoirs through their ability to capture and store anions. A schematic diagram illustrates the anion storage mechanism of PbS QDs as functional layers in memristors (Figure 8). In the initial state, ions are randomly distributed throughout the material (Figure 8a). When a positive voltage is applied to the bottom electrode, cations migrate toward the top electrode, while the intermediate QD layer stores anions, thereby facilitating cation accumulation at the functional layer/QD interface and promoting CF formation (Figure 8b). When the voltage polarity is reversed, cations and anions migrate in opposite directions at this interface, enabling efficient filament dissolution (Figure 8c). This reservoir effect directs CF growth and, in synergy with local electric field enhancement, significantly reduces the variability of switching voltages. Therefore, it provides a fundamental mechanism for the regulation of high-performance memristor operation.

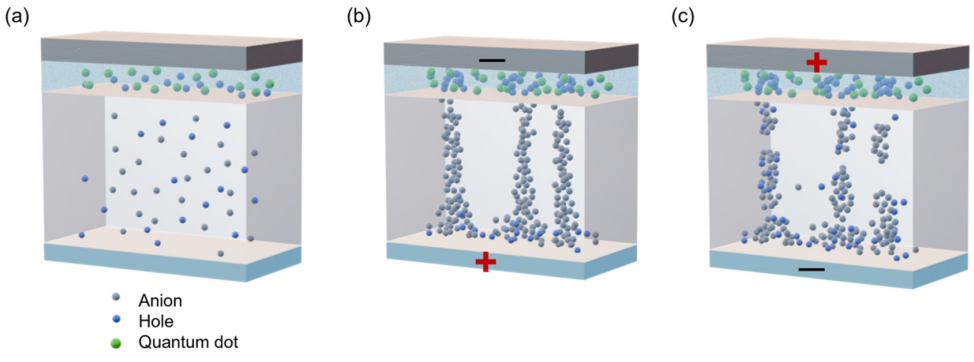


Figure 8. Schematic diagram of the resistive switching behavior: (**a**) initial state, (**b**) LRS, and (**c**) HRS.

4. Photosensitive Effect and Applications of PbS QDs

PbS QDs exhibit broadband absorption spanning the visible to near-infrared region, and their bandgap can be tuned through the quantum confinement effect [89–91]. These characteristics enable efficient photocarrier generation, separation, and controlled transport, thereby improving optically modulated switching in memristors [92–94].

Research on PbS QD-based photomemristors has progressed rapidly. In 2025, Lin et al. developed a CuSCN/PbS QD heterojunction device (Figure 9a,b) that exploits the broadband absorption of PbS QDs to achieve a panchromatic response from the ultraviolet to the near-infrared region (Figure 9c) [64]. This design enhances short-wavelength ultraviolet absorption and introduces self-rectifying behavior, which is beneficial for high-density neuromorphic computing. The device also exhibits volatile and nonlinear switching under combined optical and electrical stimulation, supporting the co-stimulation of sensing and computing.

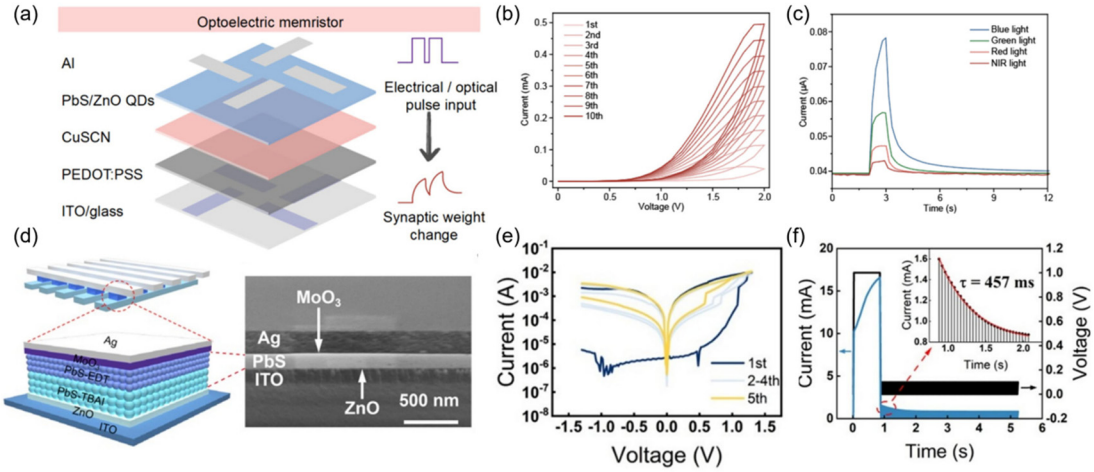


Figure 9. (**a**) Schematic illustration of the optoelectronic memristor structure. (**b**) I–V scanning curves of optoelectronic synapses. (**c**) Photoresponse of the memristor under illumination with light of different colors. Reprinted (adapted) with permission [64]. Copyright 2025, American Chemical Society. (**d**) Above: schematic diagram of the device structure of the NIR sensor array; below: structural diagram of a single pixel and SEM image of the NIR sensor. (**e**) I–V characteristic curve, scanning voltage from −1.3 V to 1.3 V and back to −1.3 V, scanning step size is 0.05 V, and the process is repeated 5 times. (**f**) Short-term plasticity (STM) characteristics. The black curve represents the pulse voltage sequence applied to the device, and the blue curve represents the response current. The inset shows a magnified view of the response current, and the red curve is an exponential fit to the experimental data. Reprinted (adapted) with permission [79]. Copyright 2025, Elsevier.

Wu et al. developed an integrated near-infrared sensing–computing system based on the photosensitivity of PbS QDs (Figure 9d) [79]. In this system, a PbS QD array directly captures target-generated near-infrared signals and enables temporal conversion and recognition of 5 × 4 digital images, achieving an entity recognition accuracy of more than 88%. This architecture uses PbS QD sensors as the input layer for memory–computing integration, thereby avoiding the preprocessing steps required in conventional vision systems and enabling direct target perception. The system's performance is attributed both to the highly uniform arrangement of PbS QDs arrays and to the material's exceptional near-infrared photonic response characteristics. In combination with the state separation characteristics of ZnO memristors, efficient target recognition is achieved (Figure 9e,f). Experimental results further confirm that PbS QDs enable in situ optical signal conversion and reliable signal input, which form the basis for direct detection capability.

The outstanding photosensitivity of PbS QDs supports the monolithic integration of light sensing, non-volatile storage, and synaptic computing, demonstrating considerable po-

tential for applications in neuromorphic computing, NIR sensing, and sensory–computing convergence [95].

5. Application of PbS QDs in Artificial Synapses

Artificial synapses (Figure 10a,b) [52], as the fundamental units of neuromorphic systems, require key characteristics such as controllable plasticity, low power consumption, fast response, and compatibility with integrated device architectures [96–98]. Continuous advances in functional materials and device structures have steadily improved the performance of artificial synapses and expanded their application scope [99–102]. Owing to their excellent optoelectronic properties, tunable bandgap, and high carrier mobility, PbS QDs provide a promising platform for the development of multifunctional and low-power artificial synapses [68,103,104]. As a result, PbS QDs have become important candidates for optoelectronic and memristive synaptic devices [105].

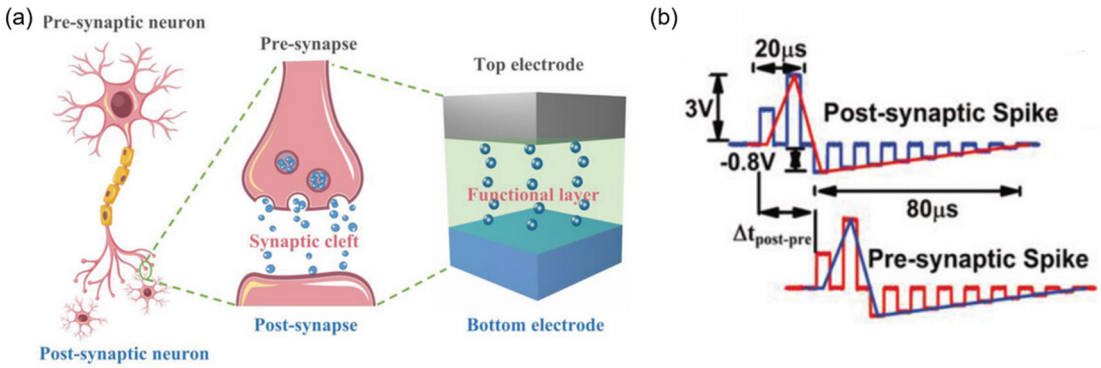


Figure 10. (**a**) Schematic illustration of the connection between a biological synapse and a memristor device for an artificial synapse. (**b**) Double-triangular pulse sequences acting as presynaptic and postsynaptic spikes. Reprinted (adapted) with permission [52]. Copyright 2023, Wiley-VCH.

PbS QDs show considerable potential for expanding the functionality of artificial synapses. Yan et al. (2018) fabricated Ag/Ga_2O_3/NQDs/Pt memristors and exploited the neuromorphic characteristics of PbS QDs to emulate synaptic behaviors, including long-term potentiation/depression (LTP/LTD), spike-timing-dependent plasticity (STDP), and paired-pulse facilitation (PPF) (Figure 11a,b) [48]. The STDP response was achieved under 200 ns pulses, corresponding to a speed approximately 10^5 times higher than that of biological synapses, which indicates strong potential for ultrafast neuromorphic computing. Subsequently, Li et al. (2019) developed a ZnO/PbS heterojunction device (Figure 11c), in which QDs promoted interfacial carrier transfer and photon-regulated oxygen vacancy modulation [77]. This photon-controlled device realized both excitatory and inhibitory synaptic functions (Figure 11d,e) with ultralow energy consumption of 4 pJ for optical modulation and 80 pJ for electrical modulation, and it achieved a recognition accuracy of 67 ± 6% in photon-modulated classification of not MNIST images. Further progress was reported by Wu et al. (2023), who developed a MoS_2/PbS QD device with nonlinear response and short-term memory, in which hole trapping by QDs enabled temporal information processing through the PPF effect [54]. More recently, Lin et al. (2025) constructed a PbS QD/CuSCN p-i-n memristor with a rectification ratio greater than 500, using the built-in electric field to enhance carrier separation [64]. This device converted 4-bit optical sequences into 16 distinct electrical states for spatiotemporal signal processing, while surface charge dynamics enabled synaptic plasticity and multibit storage (Figure 11f), thereby providing a basis for physical reservoir computing.

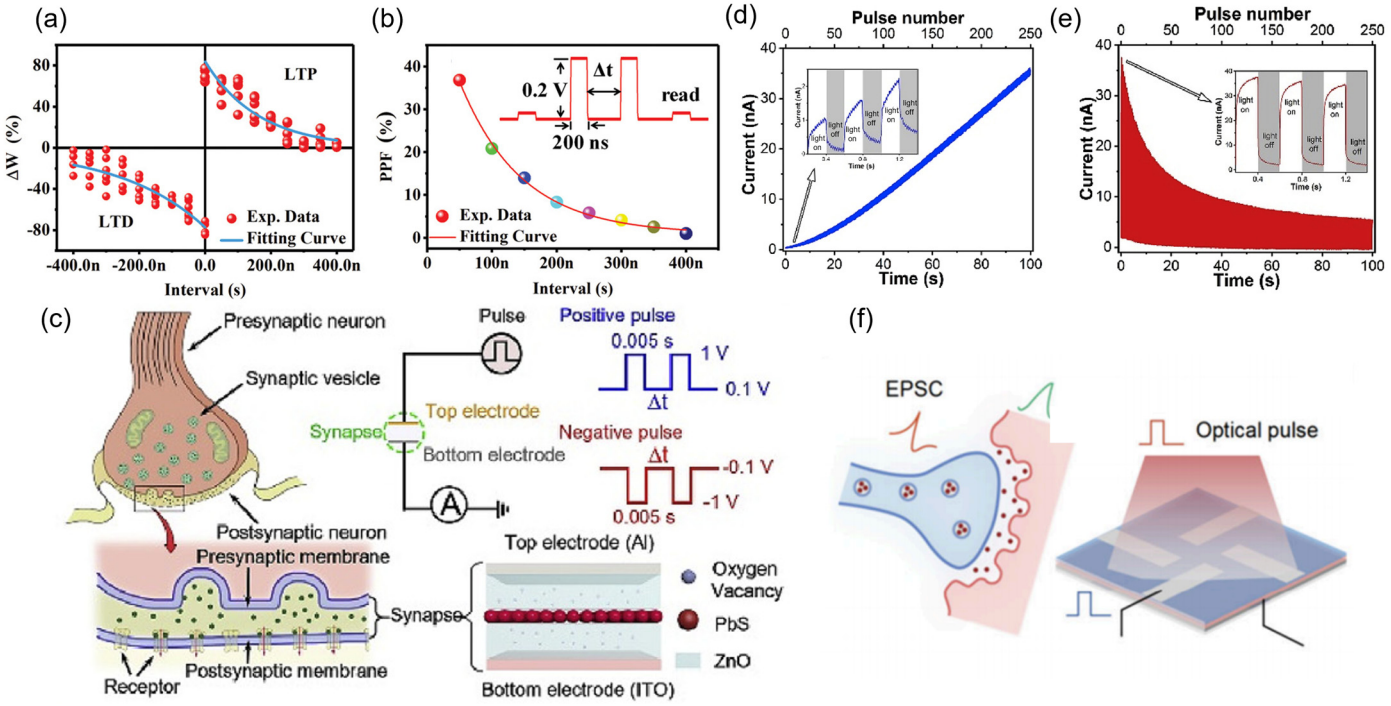


Figure 11. (**a**) STDP characteristics of MDs. (**b**) PPF characteristics of MDs and the waveform used for PPF measurement. Reprinted (adapted) with permission [48]. Copyright 2019, Wiley-VCH. (**c**) Schematic illustration of the biological synapse structure and the ZnO/PbS artificial synapse. (**d**) Emulated excitatory postsynaptic current (EPSC) plasticity using UV light pulses (0.2 s duration with 0.2 s interval). (**e**) Emulated inhibitory postsynaptic current (IPSC) plasticity using IR light pulses (0.2 s duration with 0.2 s interval). Reprinted (adapted) with permission [77]. Copyright 2019, Elsevier. (**f**) Schematic illustration of the biological synapses and optoelectronic memristor. Reprinted (adapted) with permission. Reprinted (adapted) with permission [64]. Copyright 2025, American Chemical Society.

PbS QDs provide a promising platform for improving artificial synapse performance and broadening application scenarios because of their tunable photoelectric properties, structural adaptability, and integration compatibility [106,107]. The results of existing studies have demonstrated that they can effectively alleviate several key limitations of conventional optoelectronic and memristive synapses, particularly in terms of energy efficiency, broadband response, and functional diversity [108]. These advances further promote the development of neuromorphic computing, intelligent perception, and brain–computer interfaces [109–111].

6. Summary and Outlook

In this review, we systematically summarize the key advantages of PbS QDs, including a tunable bandgap, pronounced quantum confinement, high absorption coefficient, and strong environmental stability, all of which provide the basis for their memristive applications. Their synthesis strategies can be broadly classified into top-down and bottom-up approaches. In addition, the quantum confinement effect, quasi-spherical structure, and abundant surface Pb-DBs of PbS QDs further establish them as an attractive platform for high-performance computing hardware.

Two main mechanisms are responsible for the improvement in memristor performance: (1) local electric field enhancement directs conductive filament growth through field convergence around QDs, thereby improving switching stability; (2) surface Pb-DBs dynamically stabilize the operating voltage by capturing anions such as N^{3-} and O^{2-}.

The synergy between these two mechanisms results in concentrated threshold voltages, extended retention, high endurance, and low power consumption, which together promote applications in non-volatile memory, pattern recognition, and neuromorphic synapses.

Performance test data of existing PbS QD-based memristors demonstrate exceptional storage performance and bionic synaptic reliability under ambient conditions: switching ratios across different device architectures range from 10^{10} to 10^{6}, with some laminated modified devices achieving stable write erase cycles up to 10^{9} times; most devices exhibit non-volatile data retention durations of 10^{3}–10^{4} s while reliably reproducing classical synaptic plasticity behaviors such as EPSC, LTP, and STDP. These superior properties stem from the localized electric field enhancement effect of PbS QDs and their abundant surface dangling bonds that serve as effective charge-trapping sites—effectively confining free carriers while preventing random nucleation and excessive extension of CFs, thus meeting requirements for non-volatile storage and neuromorphic computing under ambient conditions. However, lead is a toxic heavy metal; QDs are prone to ligand dissociation and lead ion leaching in bodily fluids and physiological environments, exhibiting poor biocompatibility that limits their applicability in medical applications like implantable neural devices or living-body bioelectronic chips [112]. Additionally, PbS QDs possess large specific surface areas and abundant unsaturated surface bonds, whereas traditional long-chain organic ligands demonstrate weak binding stability [113], compromising environmental tolerance: synergistic effects of moisture and oxygen in humid environments induce oxide formation and sulfate hetero-defects on the QD surface [114]; high temperatures accelerate thermal migration and agglomeration; intense light exposure introduces additional photogenerated carriers that disrupt ion transport [115]—all three extreme conditions cause SET/RESET threshold voltage drift, increased resistance state dispersion, and significant degradation of data retention performance. It is evident that introducing an oxide/polymer composite interlayer enables precise control over the microstructure of PbS QD film interfaces, significantly enhancing both device cycle durability and charge retention performance. This finding provides experimental evidence for further improving thermal and moisture resistance through ligand passivation and inorganic encapsulation to isolate water and oxygen [116,117], offering valuable insights for advancing the practical development of near-infrared optoelectronic integrated memristive devices and computing chips.

In summary, PbS QDs enable precise modulation of memristor performance and offer distinct functional advantages. High-performance devices based on these materials are expected to accelerate progress in information technology, artificial intelligence, and the semiconductor industry.

Funding: This research was funded by the Natural Science Foundation of Shandong Province (ZR2023QA095) and the Fundamental Research Program of Shanxi Province, China (Grant No. 202303021222115).

Institutional Review Board Statement: Not applicable.

Informed Consent Statement: Not applicable.

Data Availability Statement: Data are contained within the article.

Conflicts of Interest: The authors declare no conflict of interest.

References

1. Lee, Y.; Park, H.-L.; Kim, Y.; Lee, T.-W. Organic Electronic Synapses with Low Energy Consumption. *Joule* **2021**, *5*, 794–810. [CrossRef]
2. Wang, W.; Wang, Y.; Yin, F.; Niu, H.; Shin, Y.-K.; Li, Y.; Kim, E.-S.; Kim, N.-Y. Tailoring Classical Conditioning Behavior in TiO2 Nanowires: ZnO QDs-Based Optoelectronic Memristors for Neuromorphic Hardware. *Nano-Micro Lett.* **2024**, *16*, 133. [CrossRef] [PubMed]

3. Park, S.; Liao, Z.; Ibarlucea, B.; Qi, H.; Lin, H.; Becker, D.; Melidonie, J.; Zhang, T.; Sahabudeen, H.; Baraban, L.; et al. Two-Dimensional Boronate Ester Covalent Organic Framework Thin Films with Large Single Crystalline Domains for a Neuromorphic Memory Device. *Angew. Chem. Int. Ed.* **2020**, *59*, 8218–8224. [CrossRef]
4. Zhang, B.; Chen, W.; Zeng, J.; Fan, F.; Gu, J.; Chen, X.; Yan, L.; Xie, G.; Liu, S.; Yan, Q.; et al. 90% Yield Production of Polymer Nano-Memristor for in-Memory Computing. *Nat. Commun.* **2021**, *12*, 1984. [CrossRef]
5. Zhang, G.; Song, Z.; Zhang, W.; Chen, X.; Huang, S.; Dong, Y. Survey of Storage Systems in High Performance Computing. *CCF Trans. High Perform. Comput.* **2025**, *8*, 254–274. [CrossRef]
6. Wang, S.; Liu, L.; Gan, L.; Chen, H.; Hou, X.; Ding, Y.; Ma, S.; Zhang, D.W.; Zhou, P. Two-Dimensional Ferroelectric Channel Transistors Integrating Ultra-Fast Memory and Neural Computing. *Nat. Commun.* **2021**, *12*, 53. [CrossRef]
7. Khwa, W.-S.; Wen, T.-H.; Hsu, H.-H.; Huang, W.-H.; Chang, Y.-C.; Chiu, T.-C.; Ke, Z.-E.; Chin, Y.-H.; Wen, H.-J.; Hsu, W.-T.; et al. A Mixed-Precision Memristor and SRAM Compute-in-Memory AI Processor. *Nature* **2025**, *639*, 617–623. [CrossRef]
8. Wen, T.-H.; Hung, J.-M.; Huang, W.-H.; Jhang, C.-J.; Lo, Y.-C.; Hsu, H.-H.; Ke, Z.-E.; Chen, Y.-C.; Chin, Y.-H.; Su, C.-I.; et al. Fusion of Memristor and Digital Compute-in-Memory Processing for Energy-Efficient Edge Computing. *Science* **2024**, *384*, 325–332. [CrossRef]
9. An, H.; Li, Y.; Ren, Y.; Wan, Y.; Wang, W.; Sun, Z.; Zhong, J.; Peng, Z. High-Performance Flexible Resistive Random-Access Memory Based on SnS_2 Quantum Dots with a Charge Trapping/de-Trapping Effect. *Nanoscale* **2024**, *16*, 12142–12148. [CrossRef] [PubMed]
10. Zhang, C.; Li, Y.; Ma, C.; Zhang, Q. Recent Progress of Organic–Inorganic Hybrid Perovskites in RRAM, Artificial Synapse, and Logic Operation. *Small Sci.* **2022**, *2*, 2100086. [CrossRef] [PubMed]
11. Jeong, H.; Han, S.; Park, S.-O.; Kim, T.R.; Bae, J.; Jang, T.; Cho, Y.; Seo, S.; Jeong, H.-J.; Park, S.; et al. Self-Supervised Video Processing with Self-Calibration on an Analogue Computing Platform Based on a Selector-Less Memristor Array. *Nat. Electron.* **2025**, *8*, 168–178. [CrossRef]
12. Xia, Z.; Sun, X.; Wang, Z.; Meng, J.; Jin, B.; Wang, T. Low-Power Memristor for Neuromorphic Computing: From Materials to Applications. *Nano-Micro Lett.* **2025**, *17*, 217. [CrossRef]
13. Jin, B.; Wang, Z.; Wang, T.; Meng, J. Memristor-Based Artificial Neural Networks for Hardware Neuromorphic Computing. *Research* **2025**, *8*, 0758. [CrossRef] [PubMed]
14. Sung, C.; Hwang, H.; Yoo, I.K. Perspective: A Review on Memristive Hardware for Neuromorphic Computation. *J. Appl. Phys.* **2018**, *124*, 151903. [CrossRef]
15. Chua, L. Memristor-The Missing Circuit Element. *IEEE Trans. Circuit Theory* **1971**, *18*, 507–519. [CrossRef]
16. Gao, K.; Sun, B.; Cao, Z.; Wang, M.; Zhang, J.; Wang, K.; Zhou, G.; Lu, Z.; Shao, J. Brain-Inspired Computing Based on Large-Scale Memristor Crossbar Arrays. *Adv. Funct. Mater.* **2025**, *36*, e28309. [CrossRef]
17. Bharathi, M.; Wang, Z.; Guo, B.; Balraj, B.; Li, Q.; Shuai, J.; Guo, D. Memristors: Understanding, Utilization and Upgradation for Neuromorphic Computing. *Nano* **2020**, *15*, 2030005. [CrossRef]
18. Liu, Z.; Gao, C.; Yang, J.; Chen, Z.; Li, E.; Li, J.; Li, M.; Zhang, J. Memristor Devices for Next-Generation Computing: From Performance Optimization to Application-Specific Co-Design. *Int. J. Extreme Manuf.* **2026**, *8*, 012004. [CrossRef]
19. Shooshtari, M.; Serrano-Gotarredona, T.; Linares-Barranco, B. Review of Memristors for In-Memory Computing and Spiking Neural Networks. *Adv. Intell. Syst.* **2026**, *8*, e202500806. [CrossRef]
20. Lian, H.; Cheng, X.; Hao, H.; Han, J.; Lau, M.-T.; Li, Z.; Zhou, Z.; Dong, Q.; Wong, W.-Y. Metal-Containing Organic Compounds for Memory and Data Storage Applications. *Chem. Soc. Rev.* **2022**, *51*, 1926–1982. [CrossRef]
21. Mao, Q.; Zhu, Z.; Meng, J.; Wang, T. Intelligent Flexible Memristors for Artificial Synapses and Neuromorphic Computing. *FlexMat* **2025**, *2*, 188–203. [CrossRef]
22. Tiw, P.J.; Yuan, R.; Zhang, T.; Yu, L.; Yang, Y. An End-to-End Memristive Hardware System Based on Single-Spike Coding for Human–Machine Interfaces. *Nat. Electron.* **2026**, *9*, 225–236. [CrossRef]
23. Lee, J.W.; Han, J.; Kang, B.; Hong, Y.J.; Lee, S.; Jeon, I. Strategic Development of Memristors for Neuromorphic Systems: Low-Power and Reconfigurable Operation. *Adv. Mater.* **2025**, *37*, 2413916. [CrossRef]
24. Dang, B.; Zhang, T.; Meng, F.; Liu, K.; Yu, L.; Zhang, Q.; Wu, S.; Gu, L.; Huang, R.; Yang, Y. Spiking Neural Networks with Fatigue Spike-Timing-Dependent Plasticity Learning Using Hybrid Memristor Arrays. *Nat. Electron.* **2026**, *9*, 213–224. [CrossRef]
25. Wan, W.; Kubendran, R.; Schaefer, C.; Eryilmaz, S.B.; Zhang, W.; Wu, D.; Deiss, S.; Raina, P.; Qian, H.; Gao, B.; et al. A Compute-in-Memory Chip Based on Resistive Random-Access Memory. *Nature* **2022**, *608*, 504–512. [CrossRef] [PubMed]
26. Liao, K.; Lei, P.; Tu, M.; Luo, S.; Jiang, T.; Jie, W.; Hao, J. Memristor Based on Inorganic and Organic Two-Dimensional Materials: Mechanisms, Performance, and Synaptic Applications. *ACS Appl. Mater. Interfaces* **2021**, *13*, 32606–32623. [CrossRef]
27. Rehman, M.M.; Samad, Y.A.; Gul, J.Z.; Saqib, M.; Khan, M.; Shaukat, R.A.; Chang, R.; Shi, Y.; Kim, W.Y. 2D Materials-Memristive Devices Nexus: From Status Quo to Impending Applications. *Prog. Mater. Sci.* **2025**, *152*, 101471. [CrossRef]
28. Kagan, C.R.; Bassett, L.C.; Murray, C.B.; Thompson, S.M. Colloidal Quantum Dots as Platforms for Quantum Information Science. *Chem. Rev.* **2021**, *121*, 3186–3233. [CrossRef] [PubMed]

29. Kim, H. Halide Perovskite Quantum Dots Form a Scalable Unified Platform for Resistive Memories, Crossbar Networks, Neuromorphic Synapses, and Field Effect Transistors. *Adv. Mater. Interfaces* **2025**, *12*, e00506. [CrossRef]
30. Zhao, K.; Zhang, C.; Chen, Q.; Wang, K.; Qian, N.; Wang, X.; He, H.; Chen, Y. MXene Quantum Dots Covalently Modified with Poly [1,4-diethynylbenzene- *Alt* -spiropyran] for Analog-Type Optoelectronic Dual-Response Memristor. *Adv. Mater. Technol.* **2025**, *10*, 2401944. [CrossRef]
31. Youngblood, N.; Ríos, C.; Pernice, W.; Bhaskaran, H. Integrated Optical Memristors. *Nature* **2023**, *17*, 561–572. [CrossRef]
32. Liu, X.; Ren, S.; Li, Z.; Guo, J.; Yi, S.; Yang, Z.; Hao, W.; Li, R.; Zhao, J. Flexible Transparent High-Efficiency Photoelectric Perovskite Resistive Switching Memory. *Adv. Funct. Mater.* **2022**, *32*, 2202951. [CrossRef]
33. Bera, J.; Betal, A.; Sharma, A.; Shankar, U.; Rath, A.K.; Sahu, S. CdSe Quantum Dot-Based Nanocomposites for Ultralow-Power Memristors. *ACS Appl. Nano Mater.* **2022**, *5*, 8502–8510. [CrossRef]
34. Kim, D.H.; Wu, C.; Park, D.H.; Kim, W.K.; Seo, H.W.; Kim, S.W.; Kim, T.W. Flexible Memristive Devices Based on InP/ZnSe/ZnS Core–Multishell Quantum Dot Nanocomposites. *ACS Appl. Mater. Interfaces* **2018**, *10*, 14843–14849. [CrossRef]
35. Mondal, P.; Sathiyamani, S.; Das, S.; Viswanatha, R. Electronic Structure Study of Dual-Doped II–VI Semiconductor Quantum Dots towards Single-Source White Light Emission. *Nanoscale* **2023**, *15*, 15288–15297. [CrossRef] [PubMed]
36. Williams, K.R.; Diroll, B.T.; Watkins, N.E.; Rui, X.; Brumberg, A.; Klie, R.F.; Schaller, R.D. Synthesis of Type I PbSe/CdSe Dot-on-Plate Heterostructures with Near-Infrared Emission. *J. Am. Chem. Soc.* **2019**, *141*, 5092–5096. [CrossRef] [PubMed]
37. Dutta, A.; Almutairi, A.S.; Joseph, J.P.; Baev, A.; Petrou, A.; Zeng, H.; Prasad, P.N. Exploring Magneto-optic Properties of Colloidal Two-dimensional Copper-doped CdSe Nanoplatelets. *Nanophotonics* **2022**, *11*, 5143–5152. [CrossRef]
38. Mondal, P.; Chakraborty, S.; Grandhi, G.K.; Viswanatha, R. Copper Doping in II–VI Semiconductor Nanocrystals: Single-Particle Fluorescence Study. *J. Phys. Chem. Lett.* **2020**, *11*, 5367–5372. [CrossRef]
39. Fang, F.; Zhong, H.; Hao, J.; Chen, S.; Cheng, S.; Cao, T.; Zhu, H.; Tang, Y.; Pan, G.; Sun, K.; et al. Core-shell Structure Induced Surface Reconstruction of PbS Quantum Dots toward High-detectivity Short-wave Infrared Photodetectors. *InfoScience* **2026**, *3*, e70003. [CrossRef]
40. Zhao, X.; Li, M.; Ma, T.; Yan, J.; Khalaf, G.M.G.; Chen, C.; Hsu, H.-Y.; Song, H.; Tang, J. Stable PbS Colloidal Quantum Dot Inks Enable Blade-Coating Infrared Solar Cells. *Front. Optoelectron.* **2023**, *16*, 27. [CrossRef]
41. Chen, Z.; Li, Z.; Li, F.; Huo, J.; Meng, X.; Ma, S.; Zhu, W.; Guo, F.; Hu, J.-H.; Wu, K. Switchable Near-Infrared Photoluminescence of PbS Quantum Dots through Light and Heat Modulated Hole Transfer to Spiropyran Molecules. *Nano Res.* **2024**, *17*, 10483–10489. [CrossRef]
42. Das, H.; Xu, Q.; Datta, P. Effect of ZnS and PbS Shell on Mem-Behavior of CdS Quantum Dots. *J. Mater. Sci. Mater. Electron.* **2021**, *32*, 7049–7060. [CrossRef]
43. Pathania, S.; Hmar, J.J.L.; Kumar, V.; Verma, O.N.; Kumar, T.; Paulsamy, C. Gold (Au)-Doped Lead Sulfide-Polyvinyl Alcohol (PbS-PVA) Nanocomposites for High-Performance, Flexible Memristors. *J. Electron. Mater.* **2022**, *51*, 4964–4977. [CrossRef]
44. Sarma, S. Possible Application of Lead Sulfide Quantum Dot in Memory Device. *J. Polym. Eng.* **2016**, *36*, 293–297. [CrossRef]
45. Zheng, J.; Cheng, B.; Wu, F.; Su, X.; Xiao, Y.; Guo, R.; Lei, S. Modulation of Surface Trap Induced Resistive Switching by Electrode Annealing in Individual PbS Micro/Nanowire-Based Devices for Resistance Random Access Memory. *ACS Appl. Mater. Interfaces* **2014**, *6*, 20812–20818. [CrossRef]
46. Li, Z.; Li, M.; Zhu, T.; Li, B.; Wang, Z.; Shao, S.; Deng, Z.; Zhao, X.; Liu, C.; Zhao, J. Flexible Printed Ultraviolet-to-Near-Infrared Broadband Optoelectronic Carbon Nanotube Synaptic Transistors for Fast and Energy-Efficient Neuromorphic Vision Systems. *Small Methods* **2024**, *8*, 2400359. [CrossRef]
47. Wulandari, R.D.; Yin, D.; Septianto, R.D.; Izawa, S.; Iwasa, Y.; Bisri, S.Z.; Majima, Y. Molecularly-Anchored Single PbS Quantum Dots as Resonant Tunnelling Transistors. *Nanoscale* **2025**, *17*, 5672–5680. [CrossRef]
48. Yan, X.; Pei, Y.; Chen, H.; Zhao, J.; Zhou, Z.; Wang, H.; Zhang, L.; Wang, J.; Li, X.; Qin, C.; et al. Self-Assembled Networked PbS Distribution Quantum Dots for Resistive Switching and Artificial Synapse Performance Boost of Memristors. *Adv. Mater.* **2019**, *31*, 1805284. [CrossRef]
49. Younis, A.; Hu, L.; Sharma, P.; Lin, C.; Mi, Y.; Guan, X.; Zhang, D.; Wang, Y.; He, T.; Liu, X.; et al. Enhancing Resistive Switching Performance and Ambient Stability of Hybrid Perovskite Single Crystals via Embedding Colloidal Quantum Dots. *Adv. Funct. Mater.* **2020**, *30*, 2002948. [CrossRef]
50. Sun, Y.; Gao, H.; Wu, S.; Duan, Y.; Qian, M.; Guo, J.; Yang, M.; Ma, X.; Yang, Y. The Influence of Device Structure on Resistance Switching in PbS QDs Film Inserted RRAM. *Appl. Phys. Lett.* **2022**, *121*, 032104. [CrossRef]
51. Duan, Y.; Gao, H.; Guo, J.; Yang, M.; Yu, Z.; Shen, X.; Wu, S.; Sun, Y.; Ma, X.; Yang, Y. Effect of Nitrogen Capture Ability of Quantum Dots on Resistive Switching Characteristics of AlN-Based RRAM. *Appl. Phys. Lett.* **2021**, *118*, 013501. [CrossRef]
52. Hao, H.; Yan, L.; Wang, M.; Cao, Y.; He, J.; Yang, Y. Research Process of Carbon Dots in Memristors. *Adv. Electron. Mater.* **2023**, *9*, 2201195. [CrossRef]

53. Liu, Y.; Gao, Y.; Yang, Q.; Xu, G.; Zhou, X.; Shi, G.; Lyu, X.; Wu, H.; Liu, J.; Fang, S.; et al. Breaking the Size Limitation of Directly-Synthesized PbS Quantum Dot Inks Toward Efficient Short-wavelength Infrared Optoelectronic Applications. *Angew. Chem.* **2023**, *135*, e202300396. [CrossRef]
54. Wu, G.; Zhang, Z.; Ba, K.; Zhang, X.; Zeng, J.; Bai, C.; Liu, Q.; Wang, J. Hybrid MoS_2 /PbS Quantum Dots Toward In-Sensor Reservoir Computing. *IEEE Electron Device Lett.* **2023**, *44*, 857–860. [CrossRef]
55. Dong, X.; Feng, Y.; Wang, T.; Liu, F.; Zhao, P.; Chang, A.; Luo, W.; Zhang, B.; Mulvaney, P. Binary Thiourea Precursors Enable Continuous Size Control of PbS Quantum Dots. *J. Phys. Chem. C* **2026**, *130*, 3862–3871. [CrossRef]
56. Jin, J.; Kyhm, J.; Hwang, D.K.; Lee, K.-S.; Seong, T.-Y.; Hwang, G.W. Precise Control of the Oxidation State of PbS Quantum Dots Using Rapid Thermal Annealing for Infrared Photodetectors. *ACS Appl. Nano Mater.* **2021**, *4*, 1–6. [CrossRef]
57. Clark, P.C.J.; Neo, D.C.J.; Ahumada-Lazo, R.; Williamson, A.I.; Pis, I.; Nappini, S.; Watt, A.A.R.; Flavell, W.R. Influence of Multistep Surface Passivation on the Performance of PbS Colloidal Quantum Dot Solar Cells. *Langmuir* **2018**, *34*, 8887–8897. [CrossRef]
58. Wang, C.; Wu, Q.; Wang, Y.; Wang, Z.; Li, H.; Li, X.; Chen, X.; Wang, C.; Liu, Y.; Zhang, X. P-Type PbS Quantum Dot Solar Ink via Hydrogen-Bonding Modulated Solvation for High-Efficiency Photovoltaics. *Adv. Funct. Mater.* **2024**, *34*, 2315365. [CrossRef]
59. Pinna, J.; Pili, E.; Mehrabi Koushki, R.; Gavhane, D.S.; Carlà, F.; Kooi, B.J.; Portale, G.; Loi, M.A. PbI_2 Passivation of Three Dimensional PbS Quantum Dot Superlattices Toward Optoelectronic Metamaterials. *ACS Nano* **2024**, *18*, 19124–19136. [CrossRef]
60. Wang, C.; Wang, Y.; Jia, Y.; Wang, H.; Li, X.; Liu, S.; Liu, X.; Zhu, H.; Wang, H.; Liu, Y.; et al. Precursor Chemistry Enables the Surface Ligand Control of PbS Quantum Dots for Efficient Photovoltaics. *Adv. Sci.* **2023**, *10*, 2204655. [CrossRef]
61. Wei, Y.; Ding, C.; Shi, G.; Bi, H.; Li, Y.; Li, H.; Liu, D.; Yang, Y.; Wang, D.; Chen, S.; et al. Stronger Coupling of Quantum Dots in Hole Transport Layer Through Intermediate Ligand Exchange to Enhance the Efficiency of PbS Quantum Dot Solar Cells. *Small Methods* **2024**, *8*, 2400015. [CrossRef]
62. Li, B.; Duan, Z.; Zeng, W.; Bu, Y.; Yuan, Z.; Jiang, Y.; Tai, H. Advances in PbX (X = S, Se, Te) Quantum-Dot Photodetectors. *Laser Photonics Rev.* **2026**, *20*, e01759. [CrossRef]
63. Debellis, D.; Gigli, G.; Ten Brinck, S.; Infante, I.; Giansante, C. Quantum-Confined and Enhanced Optical Absorption of Colloidal PbS Quantum Dots at Wavelengths with Expected Bulk Behavior. *Nano Lett.* **2017**, *17*, 1248–1254. [CrossRef] [PubMed]
64. Lin, J.; Wang, Z.; Lin, Q.; Sun, J.; Guo, X.; Wang, Y.; Lin, L.; Zhao, Y.; Liu, Y.; Li, D.; et al. PbS Quantum Dot-Based Optoelectronic Memristors toward Multi-Task Reservoir Computing. *J. Phys. Chem. Lett.* **2025**, *16*, 199–208. [CrossRef]
65. Ding, N.; Xu, W.; Liu, H.; Jing, Y.; Wang, Z.; Ji, Y.; Wu, J.; Shao, L.; Zhu, G.; Dong, B. Highly DUV to NIR-II Responsive Broadband Quantum Dots Heterojunction Photodetectors by Integrating Quantum Cutting Luminescent Concentrators. *Light Sci. Appl.* **2024**, *13*, 289. [CrossRef] [PubMed]
66. Xu, Q.; Meng, L.; Sinha, K.; Chowdhury, F.I.; Hu, J.; Wang, X. Ultrafast Colloidal Quantum Dot Infrared Photodiode. *ACS Photonics* **2020**, *7*, 1297–1303. [CrossRef]
67. Wang, W.; Gao, S.; Wang, Y.; Li, Y.; Yue, W.; Niu, H.; Yin, F.; Guo, Y.; Shen, G. Advances in Emerging Photonic Memristive and Memristive-Like Devices. *Adv. Sci.* **2022**, *9*, 2105577. [CrossRef]
68. Hou, Y.-X.; Li, Y.; Zhang, Z.-C.; Li, J.-Q.; Qi, D.-H.; Chen, X.-D.; Wang, J.-J.; Yao, B.-W.; Yu, M.-X.; Lu, T.-B.; et al. Large-Scale and Flexible Optical Synapses for Neuromorphic Computing and Integrated Visible Information Sensing Memory Processing. *ACS Nano* **2021**, *15*, 1497–1508. [CrossRef]
69. Yang, J.; Ling, T.; Wu, W.-T.; Liu, H.; Gao, M.-R.; Ling, C.; Li, L.; Du, X.-W. A Top–down Strategy towards Monodisperse Colloidal Lead Sulphide Quantum Dots. *Nat. Commun.* **2013**, *4*, 1695. [CrossRef]
70. Liu, Y.; Tan, L.; Fu, Y.; Tang, H.; Dai, G.-P.; Tan, L. Top-Down Synthesis of N-Type PbS Quantum Dots with High Photoluminescence Quantum Yield from Microsized Pb(OH)Cl. *J. Phys. Chem. Lett.* **2024**, *15*, 9449–9455. [CrossRef]
71. Shrestha, A.; Batmunkh, M.; Tricoli, A.; Qiao, S.Z.; Dai, S. Near-Infrared Active Lead Chalcogenide Quantum Dots: Preparation, Post-Synthesis Ligand Exchange, and Applications in Solar Cells. *Angew. Chem. Int. Ed.* **2019**, *58*, 5202–5224. [CrossRef] [PubMed]
72. Gao, Z.; Wei, J.; Hu, X.; Yang, X.; Ling, K.; Li, G.; Wu, Z.; Liu, S.; Xia, Y. Review of Narrow-Bandgap Infrared Quantum Dots Solar Cells. *Sol. RRL* **2025**, *9*, e202500640. [CrossRef]
73. Pan, Y.; Li, Y.R.; Zhao, Y.; Akins, D.L. Synthesis and Characterization of Quantum Dots: A Case Study Using PbS. *J. Chem. Educ.* **2015**, *92*, 1860–1865. [CrossRef]
74. Abramkin, D.S.; Aleksandrov, I.A.; Atuchin, V.V. Prospects of Using Self-Assembled GaN/AlN Quantum Dots for Universal Memory Elements. *J. Phys. Chem. Solids* **2025**, *207*, 112945. [CrossRef]
75. Chen, Z.; Zhang, Y.; Yu, Y.; Cao, M.; Che, Y.; Jin, L.; Li, Y.; Li, Q.; Li, T.; Dai, H.; et al. Light Assisted Multilevel Resistive Switching Memory Devices Based on All-Inorganic Perovskite Quantum Dots. *Appl. Phys. Lett.* **2019**, *114*, 181103. [CrossRef]
76. Chen, Z.; Yu, Y.; Jin, L.; Li, Y.; Li, Q.; Li, T.; Li, J.; Zhao, H.; Zhang, Y.; Dai, H.; et al. Broadband Photoelectric Tunable Quantum Dot Based Resistive Random Access Memory. *J. Mater. Chem. C* **2020**, *8*, 2178–2185. [CrossRef]
77. Li, H.; Jiang, X.; Ye, W.; Zhang, H.; Zhou, L.; Zhang, F.; She, D.; Zhou, Y.; Han, S.-T. Fully Photon Modulated Heterostructure for Neuromorphic Computing. *Nano Energy* **2019**, *65*, 104000. [CrossRef]

78. Sarma, S.; Mothudi, B.M.; Dhlamini, M.S. Unipolar Resistive Switching Behaviour of Copper Doped Polyvinyl Alcohol/Lead Sulphide Quantum Dot Device. *J. Mater. Sci. Mater. Electron.* **2016**, *27*, 3785–3790. [CrossRef]
79. Wu, R.; Pan, Y.; Hu, H.; Guo, T.; Li, F. A near Infrared Sensing Reservoir Computing System for Entity Target Recognition. *Chem. Eng. J.* **2025**, *514*, 163374. [CrossRef]
80. Deshmukh, A.P.; Patil, K.; Ogale, S.; Bhave, T. Resistive Switching in $CsPbBr_3$ (0D)/MoS_2 (2D) Heterojunction System: Trap-Controlled Space Charge Limited Transport Mechanism. *ACS Appl. Electron. Mater.* **2023**, *5*, 1536–1545. [CrossRef]
81. Li, L.; Liu, B.; Feng, J.; Hu, W.; Lin, H.; Huang, Y.; Wu, D.; Zeng, F.; Zhou, J.; Tang, X. Improved Uniformity in Resistive Switching Behaviors Based on PMMA Films with Embedded Carbon Quantum Dots. *Appl. Phys. Lett.* **2021**, *118*, 222108. [CrossRef]
82. Sharma, N.; Singh, K.; Tripathi, C.C.; Bera, M.K. Biomemristor with Phototunable Resistive Switching Characteristics of a Neem (Azadirachta Indica)-Carbon Quantum Dots Composite Thin Film. *J. Electron. Mater.* **2023**, *52*, 3264–3280. [CrossRef]
83. Yu, T.; Fang, Y.; Chen, X.; Liu, M.; Wang, D.; Liu, S.; Lei, W.; Jiang, H.; Shafie, S.; Mohtar, M.N.; et al. Hybridization State Transition-Driven Carbon Quantum Dot (CQD)-Based Resistive Switches for Bionic Synapses. *Mater. Horiz.* **2023**, *10*, 2181–2190. [CrossRef]
84. Mishra, A.B.; Thamankar, R. Artificial Synapse Based on Carbon Quantum Dots Dispersed in Indigo Molecular Layer for Neuromorphic Applications. *APL Mater.* **2023**, *11*, 041122. [CrossRef]
85. Wang, X.; Zhu, Z.; Li, W.; Yang, L.; Zhao, J.; Wang, P.; Cui, Y.; Gao, Z.; Qu, W. Organic Memristor Based on Graphene Oxide Quantum Dots: PEDOT-PSS Composite Film. *Mater. Sci. Semicond. Process.* **2025**, *198*, 109798. [CrossRef]
86. Huang, Z.; Huang, W.; Xu, C.; Xu, Y.; Du, T.; Liu, W.; Li, J.; Xie, S.; Chen, G.; Chen, H. Bias-Switchable Volatile and Nonvolatile Multifunctional Photoelectric Memristors Based on MXene Quantum Dots for Efficient Selective Encryption-Decryption and Recognition. *Adv. Funct. Mater.* **2025**, *35*, 2502211. [CrossRef]
87. Pradhan, R.R.; Bera, J.; Betal, A.; Dagar, P.; Sahu, S. Hot Injection-Based Synthesized Colloidal CdSe Quantum Dots Embedded in Poly(4-Vinylpyridine) (PVP) Matrix Form a Nanoscale Heterostructure for a High On–Off Ratio Memory-Switching Device. *ACS Appl. Mater. Interfaces* **2021**, *13*, 25064–25071. [CrossRef]
88. Wang, L.; Li, J.; He, Q.; Zhang, Z.; Wen, D. Nonvolatile Photoelectric Memristor for Reconfigurable Boolean Logic Operation and Data Storage. *Appl. Mater. Today* **2024**, *39*, 102294. [CrossRef]
89. Torres-Gomez, N.; Garcia-Gutierrez, D.F.; Lara-Canche, A.R.; Triana-Cruz, L.; Arizpe-Zapata, J.A.; Garcia-Gutierrez, D.I. Absorption and Emission in the Visible Range by Ultra-Small PbS Quantum Dots in the Strong Quantum Confinement Regime with S-Terminated Surfaces Capped with Diphenylphosphine. *J. Alloys Compd.* **2021**, *860*, 158443. [CrossRef]
90. Zhou, X.; Ding, X.; Liu, Y.; Xu, J.; Gao, C.; Yuan, L.; Sun, X.; Liu, Z.; Ma, W. Balancing Monomer and Ionic Ligand Supply for Scalable Direct Synthesis of Short-Wavelength Infrared PbS Quantum Dot Inks. *Nano Res.* **2025**, *18*, 94907504. [CrossRef]
91. Hong, S.; Oh, D.Y.; Oh, S.J. Quantum Dot-Based Infrared Photodiodes and Image Sensors. *Trans. Electr. Electron. Mater.* **2026**, *27*, 6–22. [CrossRef]
92. Shultz, A.; Liu, B.; Gong, M.; Hernandez, F.C.R.; Wu, J. Pixel Geometry Effect on PbS Quantum Dot/Graphene Nanohybrid Broadband Photodetectors. *Adv. Opt. Mater.* **2024**, *12*, 2302675. [CrossRef]
93. Yin, X.; Zhang, C.; Guo, Y.; Yang, Y.; Xing, Y.; Que, W. PbS QD-Based Photodetectors: Future-Oriented near-Infrared Detection Technology. *J. Mater. Chem. C* **2021**, *9*, 417–438. [CrossRef]
94. Gan, J.; Yu, M.; Hoye, R.L.Z.; Musselman, K.P.; Li, Y.; Liu, X.; Zheng, Y.; Zu, X.; Li, S.; MacManus-Driscoll, J.L.; et al. Defects, Photophysics and Passivation in Pb-Based Colloidal Quantum Dot Photovoltaics. *Mater. Today Nano* **2021**, *13*, 100101. [CrossRef]
95. Chen, S.; Zhong, H.; Wang, X.; Pan, G.; Tang, H.; Fang, F.; Wu, J.; Wang, W.; Xu, L.; Tang, J.; et al. Hybrid-Size Quantum Dots in Hole Transport Layer Depress Dark Current Density of Short-Wave Infrared Photodetectors. *ACS Photonics* **2025**, *12*, 879–888. [CrossRef]
96. Jeong, U.-C.; Ro, J.-S.; Park, H.-L.; Lee, T.-W. Modulating Short-Term and Long-Term Plasticity of Polymer-Based Artificial Synapses for Neuromorphic Computing and Beyond. *Neuromorphic Comput. Eng.* **2024**, *4*, 032001. [CrossRef]
97. Tran, K.; Wang, H.; Pieters, M.; Loi, M.A. Lead Sulfide Quantum Dots for Synaptic Transistors: Modulating the Learning Timescale with Ligands. *Adv. Intell. Syst.* **2023**, *5*, 2300218. [CrossRef]
98. Liu, L.; Wang, D.; Wang, D.; Sun, Y.; Lin, H.; Gong, X.; Zhang, Y.; Tang, R.; Mai, Z.; Hou, Z.; et al. Domain Wall Magnetic Tunnel Junction-Based Artificial Synapses and Neurons for All-Spin Neuromorphic Hardware. *Nat. Commun.* **2024**, *15*, 4534. [CrossRef]
99. Ai, L.; Pei, Y.; Song, Z.; Yong, X.; Song, H.; Liu, G.; Nie, M.; Waterhouse, G.I.N.; Yan, X.; Lu, S. Ligand-Triggered Self-Assembly of Flexible Carbon Dot Nanoribbons for Optoelectronic Memristor Devices and Neuromorphic Computing. *Adv. Sci.* **2023**, *10*, 2207688. [CrossRef]
100. Mojumder, M.R.H.; Kim, S.; Yu, C. Soft Artificial Synapse Electronics. *Research* **2025**, *8*, 0582. [CrossRef] [PubMed]
101. Chen, S.; Zhang, T.; Tappertzhofen, S.; Yang, Y.; Valov, I. Electrochemical-Memristor-Based Artificial Neurons and Synapses—Fundamentals, Applications, and Challenges. *Adv. Mater.* **2023**, *35*, 2301924. [CrossRef]
102. Chandrasekaran, S.; Chang, Y.-F.; Simanjuntak, F.M. Memristor Synapse—A Device-Level Critical Review. *Nanomaterials* **2026**, *16*, 179. [CrossRef]

103. Wang, Z.; Chen, K.; Wang, Q.; Yang, J.; Qin, Z.; Hu, Y.; Shen, J.; Zhang, P.; Zhou, J.; Chen, W. Machine Learning and High-Throughput Computation-Assisted Precise Synthesis of Quantum Dots for Reliable Neuromorphic Computing. *Sci. China Mater.* **2025**, *68*, 3778–3788. [CrossRef]
104. Leng, K.; Guo, Z.; Chen, J.; Fu, Y.; Ma, R.; Yu, X.; Wang, L.; Wang, Q. PbS/$CsPbBr_3$ Heterojunction for Broadband Neuromorphic Vision Sensing. *ACS Appl. Mater. Interfaces* **2024**, *16*, 7470–7479. [CrossRef]
105. Xia, H.; Lv, L.; Ran, X.; Yuan, M.; Lan, X. Ultralow Dark Current and Broadband PbS Colloidal Quantum Dot Photodetectors. *ACS Photonics* **2026**, *13*, 2291–2301. [CrossRef]
106. Pei, Y.; Yan, L.; Wu, Z.; Lu, J.; Zhao, J.; Chen, J.; Liu, Q.; Yan, X. Artificial Visual Perception Nervous System Based on Low-Dimensional Material Photoelectric Memristors. *ACS Nano* **2021**, *15*, 17319–17326. [CrossRef] [PubMed]
107. Zhao, W.; Lin, Z.; Zhang, L.; Xu, S.; Chen, E.; Guo, T.; Ye, Y. All-Optical Synapse Enabled by CdS/PbS Nano-PN Junctions for Visual Information Processing. *ACS Photonics* **2025**, *12*, 6935–6945. [CrossRef]
108. Wang, Y.; Yin, L.; Huang, W.; Li, Y.; Huang, S.; Zhu, Y.; Yang, D.; Pi, X. Optoelectronic Synaptic Devices for Neuromorphic Computing. *Adv. Intell. Syst.* **2021**, *3*, 2000099. [CrossRef]
109. Lin, Y.; Zhang, Q.; Gao, B.; Tang, J.; Yao, P.; Li, C.; Huang, S.; Liu, Z.; Zhou, Y.; Liu, Y.; et al. Uncertainty Quantification via a Memristor Bayesian Deep Neural Network for Risk-Sensitive Reinforcement Learning. *Nat. Mach. Intell.* **2023**, *5*, 714–723. [CrossRef]
110. Zeng, J.; Zhao, J.; Bu, T.; Liu, G.; Qi, Y.; Zhou, H.; Dong, S.; Zhang, C. A Flexible Tribotronic Artificial Synapse with Bioinspired Neurosensory Behavior. *Nano-Micro Lett.* **2023**, *15*, 18. [CrossRef]
111. Yang, J.; Wang, R.; Ren, Y.; Mao, J.; Wang, Z.; Zhou, Y.; Han, S. Neuromorphic Engineering: From Biological to Spike-Based Hardware Nervous Systems. *Adv. Mater.* **2020**, *32*, 2003610. [CrossRef] [PubMed]
112. Uppala, V.V.S.; Dones Lassalle, C.Y.; Kelm, J.E.; Camp, A.M.; Ter Horst, M.A.; Esker, A.R.; Dempsey, J.L.; Madsen, L.A. Ligand Exchange and Binding at the Surface of PbS Quantum Dots Quantified Using Multimodal Magnetic Resonance. *ACS Nano* **2025**, *19*, 27246–27258. [CrossRef]
113. Sloboda, T.; Svanström, S.; Johansson, F.O.L.; Bryngelsson, E.; García-Fernández, A.; Lindblad, A.; Cappel, U.B. The Impact of Chemical Composition of Halide Surface Ligands on the Electronic Structure and Stability of Lead Sulfide Quantum Dot Materials. *Phys. Chem. Chem. Phys.* **2022**, *24*, 12645–12657. [CrossRef] [PubMed]
114. Yang, X.; Yang, J.; Khan, J.; Deng, H.; Yuan, S.; Zhang, J.; Xia, Y.; Deng, F.; Zhou, X.; Umar, F.; et al. Hydroiodic Acid Additive Enhanced the Performance and Stability of PbS-QDs Solar Cells via Suppressing Hydroxyl Ligand. *Nano-Micro Lett.* **2020**, *12*, 37. [CrossRef]
115. Jeong, Y.J.; Kim, G.-B.; Kim, M.J.; Oh, J.; Chang, J.-H.; Jeong, J.K. Improvement in Performance and Stability of PbS QD/IGZO Phototransistors Through the Introduction of Ga_2 O_3 Film for Broadband Sensor Applications. *ACS Appl. Mater. Interfaces* **2024**, *16*, 36527–36538. [CrossRef]
116. Wang, M.; Yin, C.; Du, Y.; Liu, H.; Sun, B. Aromatic Bidentate Ligand Passivation for High-Performance PbS Quantum Dot Infrared Photodetectors. *J. Phys. Chem. Lett.* **2026**, *17*, 483–492. [CrossRef]
117. Cao, Y.; Stavrinadis, A.; Lasanta, T.; So, D.; Konstantatos, G. The Role of Surface Passivation for Efficient and Photostable PbS Quantum Dot Solar Cells. *Nat. Energy* **2016**, *1*, 16035. [CrossRef]

Disclaimer/Publisher's Note: The statements, opinions and data contained in all publications are solely those of the individual author(s) and contributor(s) and not of MDPI and/or the editor(s). MDPI and/or the editor(s) disclaim responsibility for any injury to people or property resulting from any ideas, methods, instructions or products referred to in the content.